

Research Article

Open Access



High strength and ductility in partially recrystallized $\text{Fe}_{40}\text{Mn}_{20}\text{Cr}_{20}\text{Ni}_{20}$ high-entropy alloys at cryogenic temperature

Qi-Xin Ma¹ , Hui-Jun Yang^{1,2} , Zhong Wang¹ , Xiao-Hui Shi¹, Peter K. Liaw³ , Jun-Wei Qiao^{1,2}

¹College of Materials Science and Engineering, Taiyuan University of Technology, Taiyuan 030024, Shanxi, China.

²Key Laboratory of Interface Science and Engineering in Advanced Materials, Ministry of Education, Taiyuan University of Technology, Taiyuan 030024, Shanxi, China.

³Department of Materials Science and Engineering, The University of Tennessee, Knoxville, TN 37996, USA.

Correspondence to: Prof. Jun-Wei Qiao, College of Materials Science and Engineering, Taiyuan University of Technology, 79 Yingze W Ave, Wanbailin District, Taiyuan 030024, Shanxi, China. E-mail: qiaojunwei@gmail.com

How to cite this article: Ma QX, Yang HJ, Wang Z, Shi XH, Liaw PK, Qiao JW. High strength and ductility in partially recrystallized $\text{Fe}_{40}\text{Mn}_{20}\text{Cr}_{20}\text{Ni}_{20}$ high-entropy alloys at cryogenic temperature. *Microstructures* 2022;2:2022015. <https://dx.doi.org/10.20517/microstructures.2022.12>

Received: 23 May 2022 **First Decision:** 16 Jun 2022 **Revised:** 30 Jun 2022 **Accepted:** 11 Jul 2022 **Published:** 19 Jul 2022

Academic Editors: Yong Zhang, Zibin Chen **Copy Editor:** Fangling Lan **Production Editor:** Fangling Lan

Abstract

The effects of cold rolling and subsequent annealing on the microstructures and mechanical properties of $\text{Fe}_{40}\text{Mn}_{20}\text{Cr}_{20}\text{Ni}_{20}$ high-entropy alloys (HEAs) are investigated. The Cr-rich secondary phases with a tetragonal structure (σ phases) in the $\text{Fe}_{40}\text{Mn}_{20}\text{Cr}_{20}\text{Ni}_{20}$ HEAs are precipitated upon annealing at 600 °C–900 °C for 2 h. The prepared $\text{Fe}_{40}\text{Mn}_{20}\text{Cr}_{20}\text{Ni}_{20}$ HEA annealed at 800 °C for 2 h after cold rolling has a good combination of strength and elongation, with a high yield strength of 438 MPa, a high ultimate tensile strength of 676 MPa, and an excellent elongation to fracture of 32%. The mechanical properties at cryogenic temperature are better than those at room temperature. Typically, for the incompletely recrystallized alloy annealed at 700 °C, the yield strength, tensile strength, and elongation after fracture are increased by 26%, 22%, and 100%, respectively. This trend mainly depends on dislocation and twinning strengthening. The σ phases also improve the cryogenic tensile properties. Furthermore, the recrystallization kinetics of the $\text{Fe}_{40}\text{Mn}_{20}\text{Cr}_{20}\text{Ni}_{20}$ HEAs are explored to correlate with the deformation behavior.

Keywords: High-entropy alloys, mechanical properties, plastic deformation, recrystallization kinetics, cryogenic temperature



© The Author(s) 2022. **Open Access** This article is licensed under a Creative Commons Attribution 4.0 International License (<https://creativecommons.org/licenses/by/4.0/>), which permits unrestricted use, sharing, adaptation, distribution and reproduction in any medium or format, for any purpose, even commercially, as long as you give appropriate credit to the original author(s) and the source, provide a link to the Creative Commons license, and indicate if changes were made.



INTRODUCTION

High-entropy alloys (HEAs) are a new type of structural material that has attracted widespread attention in the last decade. Due to their special internal characteristics^[1-5], such as high configurational entropy^[6], large lattice distortion^[7-9] and slow atom diffusion^[10], HEAs have several compelling features, including super-high strength^[11], excellent fracture toughness^[12] and extreme corrosion resistance^[13-15]. Among newly designed HEAs, the tensile strength and ductility of single-phase face-centered-cubic (FCC) HEAs at 77 K are significantly higher than at 298 K^[4]. This feature is due to the continuous activation of a large number of twins at low temperatures whilst maintaining a high fracture toughness of up to 219 MPa·m^{1/2} (at 77 K). These characteristics endow HEAs, as new low-temperature structural materials, with a wide range of application prospects.

In order to further improve the tensile properties at cryogenic temperature, especially the low yield strength, various strengthening mechanisms have been intensively introduced, including solid solution, dislocation, second phase and phase transformation strengthening, and fine grain refinement. For example, Li *et al.* found that a strain-induced FCC to hexagonal-close-packed transformation enhances Fe₅₀Mn₃₀Co₁₀Cr₁₀ HEAs with an ultimate tensile strength (UTS) of ~870 MPa and a uniform elongation of ~75%^[1]. However, FCC HEAs are difficult to popularize due to their low yield strength and high cost, especially because they contain expensive Co and Ti elements. The development of Co-free FCC HEAs has therefore become of critical importance.

Based on current work and early findings, a low-cost four-component HEA using thermodynamic calculations was developed to adjust the phase precipitation and recrystallization kinetics. Moreover, the σ phase was employed to strengthen the low-temperature tensile properties. Due to the formation of fine σ phases in the FCC matrix, newly-developed HEAs exhibit good yield and tensile strengths of 0.52-1.02 and 0.70-1.15 GPa, respectively, and a low temperature ductility of 20%-78%. Considering the effects of the recrystallization, grain size, and secondary phase, the relationships between the microstructures, mechanical properties, and deformation mechanisms of Fe₄₀Mn₂₀Cr₂₀Ni₂₀ HEAs are investigated.

MATERIALS AND METHODS

The studied Fe₄₀Mn₂₀Cr₂₀Ni₂₀ cast ingots with dimensions of 450 × 200 × 70 mm³ and weights of ~50 kg were prepared with vacuum-induction melting equipment using pure metal elements (purity of > 99.95 wt.%). Additional elements, such as carbon and oxygen, are inevitable in the preparation for the actual industrial production. After homogenization for 1.5 h at 1200 °C, the alloy ingot was hot rolled at 1150 °C for seven passes and with a final rolling temperature of 850 °C to produce a plate with a thickness of ~7 mm, which was then water quenched. The 15 × 10 × 7 mm³ sheet cut from the hot-rolled sheet by electrical discharge machining (EDM) was cold rolled to 1.26 mm (an ~82% reduction). To prevent the specimen from bending, unidirectional rolling was selected during pre-deformation and each sample was rotated 180° for each pass. The alloy was annealed at 600, 700, 800, and 900 °C for 2 h in a preheated furnace at the corresponding temperatures and then cooled to room temperature with water.

Dog-bone-shaped tensile specimens with gauge dimensions of 1 × 10 × 3 mm³ were cut by EDM. The uniaxial tensile test was performed using an Instron 5969 testing machine with the assistance of a digital image correlation technique. Three specimens were tested with a strain rate of 1 × 10⁻³ s⁻¹ at ambient temperature (293 K) and liquid-nitrogen temperature (77 K) along the rolling direction. All tensile tests were repeated at least three times to ensure the reliability and reproducibility of the results. The cross section of the tension-fractured sample was mounted to analyze the deformed structure.

The phase identification was characterized by X-ray diffraction (XRD) using Cu K α radiation with a scanning speed of 0.02°/s. The microstructure of the annealed alloy under different conditions was characterized by optical microscopy and scanning electron microscopy (SEM) at 20 kV with a working distance of 9.1 mm and equipped with an energy-dispersive detector. A total of 10-20 SEM images were analyzed for each condition. Transmission electron microscopy (TEM) was used to investigate the crystal structures and chemical compositions of the secondary phases. Thin slices for the TEM samples were produced by mechanical polishing to a thickness of 35 μ m. Disks (3 mm) were punched out from the foils and polished in a double jet-polishing system (Tenupol-5, Struers) using an electrolyte consisting of 90 vol.% C₂H₅OH and 10 vol.% HClO₄ with a voltage of 22.5 V at -20 °C. The TEM observations were performed by employing a JEM-F200 microscope operating at 200 kV. Standard bright-field images and diffraction patterns were obtained by employing a transmission electron microscope from Philips. Electron backscattering diffraction (EBSD) was performed using a JEOL JSM-7100F scanning electron microscope at an inclination angle of 70° at 20 kV. The obtained EBSD patterns were indexed using FCC copper as the base crystal structure and analyzed by employing the commercially-available HKL Channel 5. EBSD was used to analyze the microstructures and the degree of recrystallization. The EBSD samples were mechanically polished using SiC papers and polished using an electrolyte consisting of 90 vol.% C₂H₅OH and 10 vol.% HClO₄ at 35 V for 15 s. The EBSD analysis was conducted at 25 kV with a beam size of 80 nm.

RESULTS AND DISCUSSION

Phase diagrams

The equilibrium phase diagram of the Fe₄₀Mn₂₀Cr₂₀Ni₂₀ HEA is obtained by using the equilibrium phase diagram module of JMat-Pro, as shown in [Figure 1](#). The liquidus temperature (the temperature at which a solid crystallizes during the transition from liquid cooling to a solid) of the Fe₄₀Mn₂₀Cr₂₀Ni₂₀ HEA is ~1360 °C and the solid-phase temperature (the temperature at which melting begins in an alloy) is ~1340 °C. The alloy exhibits the σ , FCC and body-centered cubic (BCC) three-phase structure when the temperature is less than 400 °C, the σ and FCC dual phases when the temperature is between 400 and 650 °C and the FCC and BCC dual phases above 650 °C. Therefore, annealing at temperatures below 900 °C can precipitate a small amount of σ phases in the alloy, hindering the growth of grain boundaries and improving the yield strength of the alloy. Accordingly, the cold-rolled samples were annealed at 600, 700, 800, and 900 °C for 2 h. Generally, the HEA is actually obtained by non-equilibrium solidification, and it is unavoidable to have a small amount of BCC phases and carbides in the solidified structure. Thus, during rapid cooling, it is highly possible to “skip” the BCC phase and carbide region to obtain the FCC and σ phases. Simultaneously, due to the participation of C atoms, very few M₂₃C₆ carbides are produced.

Microstructures of HEA after initial hot rolling and subsequent annealing

Since the alloy inevitably deviates from its nominal composition during preparation, the actual composition of the current HEA and the secondary phase was obtained by SEM-EDS elemental analysis, as shown in [Table 1](#). The design of the alloy is a new low-cost Co-free Fe₄₀Mn₂₀Cr₂₀Ni₂₀ (at.%) HEA, which can further improve its comprehensive mechanical properties while reducing the cost of the HEA. In [Table 1](#), we also detail the specific components of the secondary σ phase for a better explanation. The targeted microstructure was determined by probing the respective phase constituents of the studied alloy system annealed at particular temperatures. This process is completed by analyzing the XRD patterns of the Fe₄₀Mn₂₀Cr₂₀Ni₂₀ HEA after hot rolling and annealing at different temperatures [[Figure 2](#)]. It can be seen from the figure that the alloy after hot rolling and annealing for 2 h remains a single-phase FCC structure. When the annealing temperature reaches 600 °C, it could detect the weak diffraction peak of the precipitated phase (it is confirmed that the precipitated phase is σ). When the annealing temperature reaches 700 °C, the maximum number of diffraction peaks of the precipitated phase is detected. This trend is consistent with the SEM analysis discussed later.

Table 1. Chemical composition of matrix and precipitation of $\text{Fe}_{40}\text{Mn}_{20}\text{Cr}_{20}\text{Ni}_{20}$ HEA (at.%)

Principal composition (at.%)	Fe	Mn	Cr	Ni
Matrix	40.67	19.79	18.85	20.69
Precipitated phase	9.58	32.61	54.93	2.88

HEA: High-entropy alloy.

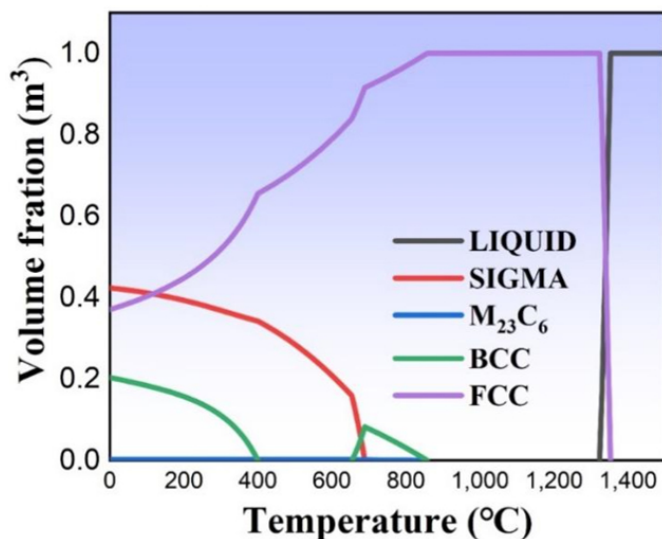


Figure 1. Equilibrium phase diagram of $\text{Fe}_{40}\text{Mn}_{20}\text{Cr}_{20}\text{Ni}_{20}$ HEA. HEA: High-entropy alloy.

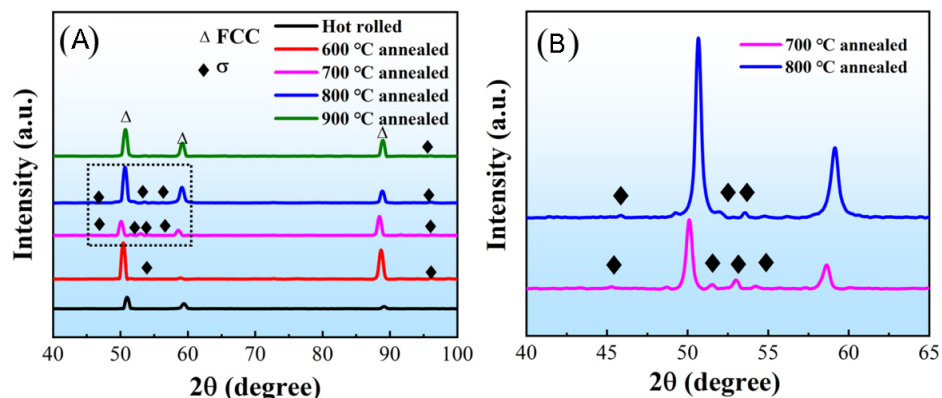


Figure 2. (A) XRD patterns of prepared $\text{Fe}_{40}\text{Mn}_{20}\text{Cr}_{20}\text{Ni}_{20}$ HEA samples in different states. (B) Enlarged view of the dotted box in (A). XRD: X-ray diffraction; HEA: high-entropy alloy.

Figure 3A shows that the hot-rolled sample has single-phase equiaxed grains with a grain size of $13.3 \mu\text{m}$. **Figure 3B-E** show the elemental distribution (SEM-EDS) diagram of the hot-rolled sample. It can be found that the alloying elements in the homogenized sample are uniformly distributed.

The SEM images of the $\text{Fe}_{40}\text{Mn}_{20}\text{Cr}_{20}\text{Ni}_{20}$ HEA after room-temperature rolling and annealing at 600°C - 900°C are shown in **Figure 4**. The backscattered electron (BSE) micrograph of the sample annealed at 600°C for 2 h after rolling showed that a large number of slip bands was still retained within the sample, indicating that the annealing temperature of 600°C could not provide sufficient energy for the sample to

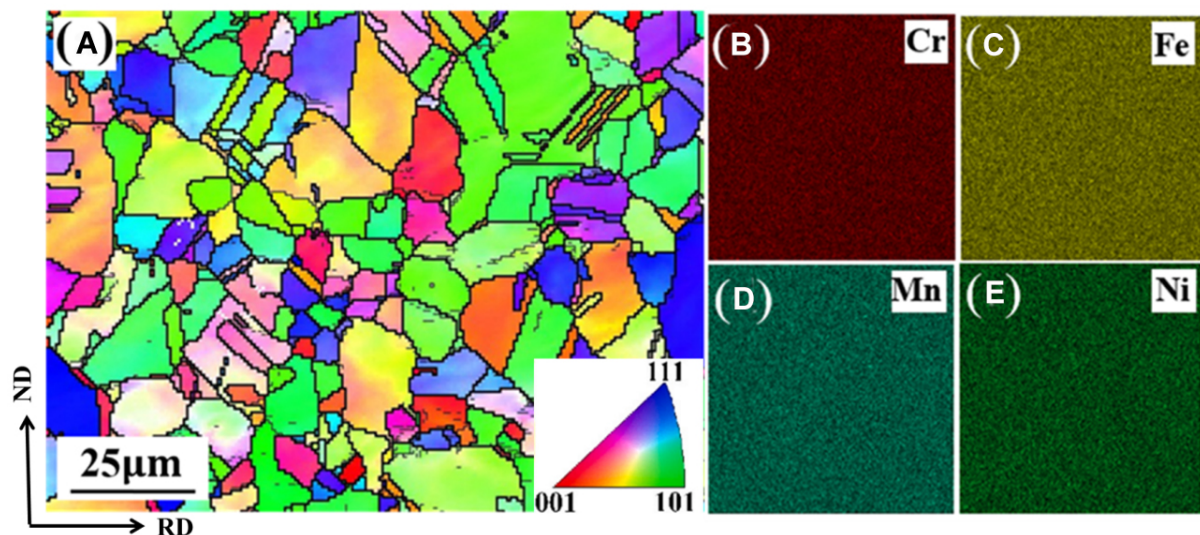


Figure 3. (A) Inverse pole figure (IPF) map of hot-rolled HEA. (B-E) EDS elemental maps of Cr, Fe, Mn, and Ni elements. HEA: High-entropy alloy.

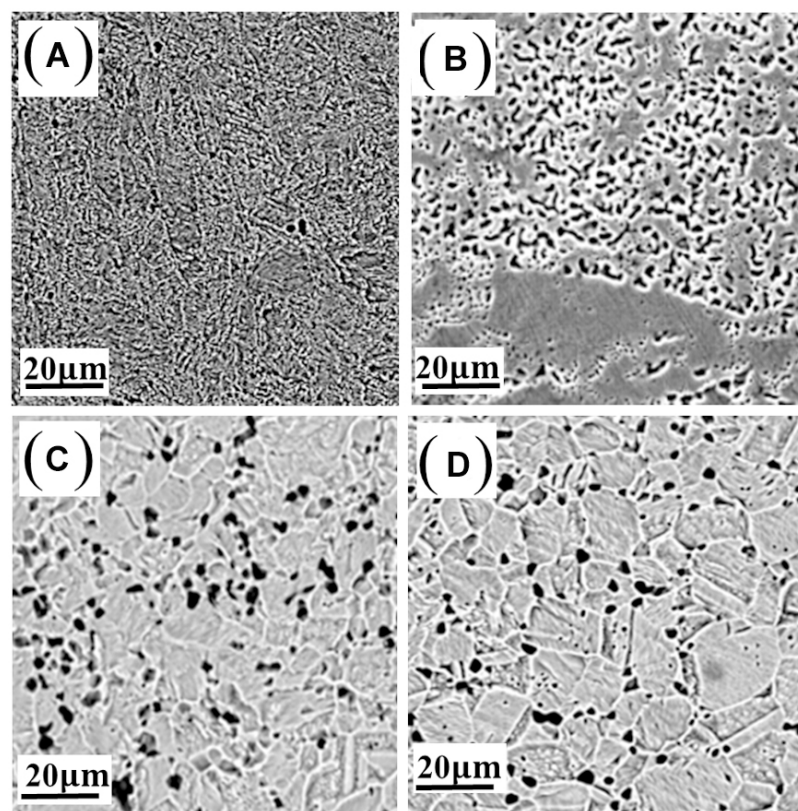


Figure 4. Microstructures of $\text{Fe}_{40}\text{Mn}_{20}\text{Cr}_{20}\text{Ni}_{20}$ HEA at different temperatures with annealing for 2 h: (A) 600 °C; (B) 700 °C; (C) 800 °C; (D) 900 °C. HEA: High-entropy alloy.

cause the alloy to recrystallize [Figure 4A]. Figure 4B shows the SEM map of the sample annealed at 700 °C for 2 h after rolling. It can be found that the FCC phase only partially recrystallized and retained a significant amount of deformation microstructures. A larger number of secondary phase particles

precipitates at the grain boundaries and inside the grains. The precipitated phase is confirmed to be a tetragonal-structured Cr-rich σ phase by the XRD and selective area electron diffraction (SAED) analysis. At higher annealing temperatures [Figure 4C and D], the alloy underwent complete recrystallization.

According to the SEM images, the grain sizes of the samples annealed at 800 and 900 °C for 2 h are 5.4 and 8.5 μm , respectively. At the four temperatures, the amount of secondary phase is largest at the annealing temperature of 700 °C and then decreases at 800 °C. The content of the precipitated phase is lowest when the annealing temperature is 600 or 900 °C. For the 700 °C specimen, the σ particles are quite populated and their size and volume fraction are 1438 nm and 18.2%, respectively. The volume fractions of the precipitated phases of 8.3%, 13.5%, and 10.4%, annealed at 600, 800, and 900 °C, respectively, were obtained by Image-Pro Plus 6.0 software. In the present study, σ -phase particles were generally found at triple points, grain boundaries and annealing twin boundaries, indicating that these locations are preferential nucleation sites for heterogeneous nucleation, as presented in Figure 4.

At the studied temperature, it is found that the precipitated phases are larger at the triple points, slightly smaller at the grain boundaries and finally smallest within the grains, as shown in the BSE micrograph of Figure 4. Under these different microstructural characteristics, the size of the precipitates is affected by both nucleation and growth. The nucleation sites of heterogeneous nucleation show different activation barriers, with the activation barriers from the lowest to the highest being triple points < grain boundaries < stacking faults < dislocations. In addition, since the grain boundaries provide a faster diffusion path than the dislocation, the precipitation at the grain boundaries should grow faster than the precipitates located at the dislocation^[16]. Therefore, the secondary phase in the recrystallized alloy is more likely to nucleate at the triple points and grain boundaries.

Incomplete recrystallization occurred in the alloy subjected to annealing at 700 °C for 2 h. As shown in Figure 4B, the incompletely recrystallized alloy is composed of fully and incompletely recrystallized grains. In order to further study the grain orientation and dislocation distribution in the incompletely recrystallized alloy, the recrystallized alloy was investigated and EBSD analysis was performed. Figure 5 shows the phase map, IPF, grain boundary map, and Kernel average misorientation (KAM) maps obtained by EBSD of the specimens after tensile fracture at low temperature. For the incomplete recrystallization of the HEA [Figure 5a1-a4], the deformation twins of the partially recrystallized samples are mainly distributed in partially recrystallized coarse grains, while in recrystallized fine grains, no twins were found within the grains. This trend can be explained by the different magnitudes of the twin critical stresses in different regions. For the complete recrystallization of the HEA [Figure 5b1-b4], the annealing temperature of 900 °C provides sufficient energy to recrystallize the alloy. Fine σ phases in the IPF diagram of EBSD are shown in Figure 5a. It is noteworthy that according to the KAM figure, the strain distribution in the partially recrystallized grain is not uniform and the local strain at grain boundaries is higher than that in the grains. In addition, the KAM value can also reflect the geometrically necessary dislocations in the alloy.

To identify the second-phase particles and their compositions, TEM studies were performed. Figure 6A shows that dislocation walls are widely available in the HEA, which reveals that there is high dislocation density within the grains. Figure 6B and C show the bright-field (BF) images of the HEA annealed at 700 °C. The BF images show a complex microstructure with multiple particles. Figure 6D shows the TEM image of the twins in a tensile specimen strained to fracture at 77 K. Moreover, twins are further verified by SAED in Figure 6E and F. The green circle taken from the BF image corresponds to the pattern of the tetragonal σ phase near the [101] zone axis [Figure 6E], which is consistent with the XRD result. In Figure 6E, the SAED patterns are indexed as a tetragonal-structured precipitate along the zone direction of [101]. Figure 6F

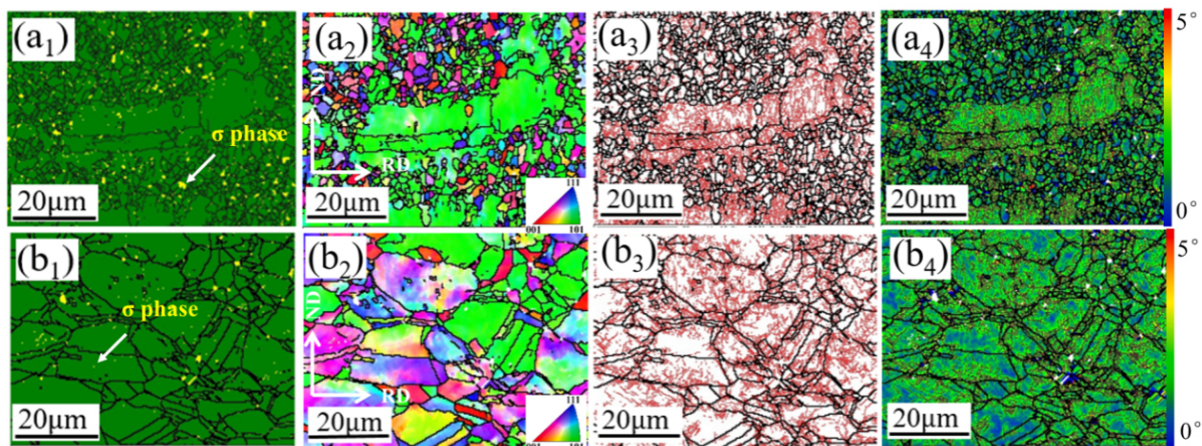


Figure 5. EBSD of $\text{Fe}_{40}\text{Mn}_{20}\text{Cr}_{20}\text{Ni}_{20}$ HEA annealed at 700 and 900 °C for 2 h after tensile fracture at cryogenic temperature: (a₁ and b₁) phase maps; (a₂ and b₂) IPF diagrams; (a₃ and b₃) grain boundary diagrams, where the black solid lines represent the large-angle grain boundaries and the red solid lines denote the twin boundaries; (a₄ and b₄) KAM maps. EBSD: Electron backscattering diffraction; HEA: high-entropy alloy.

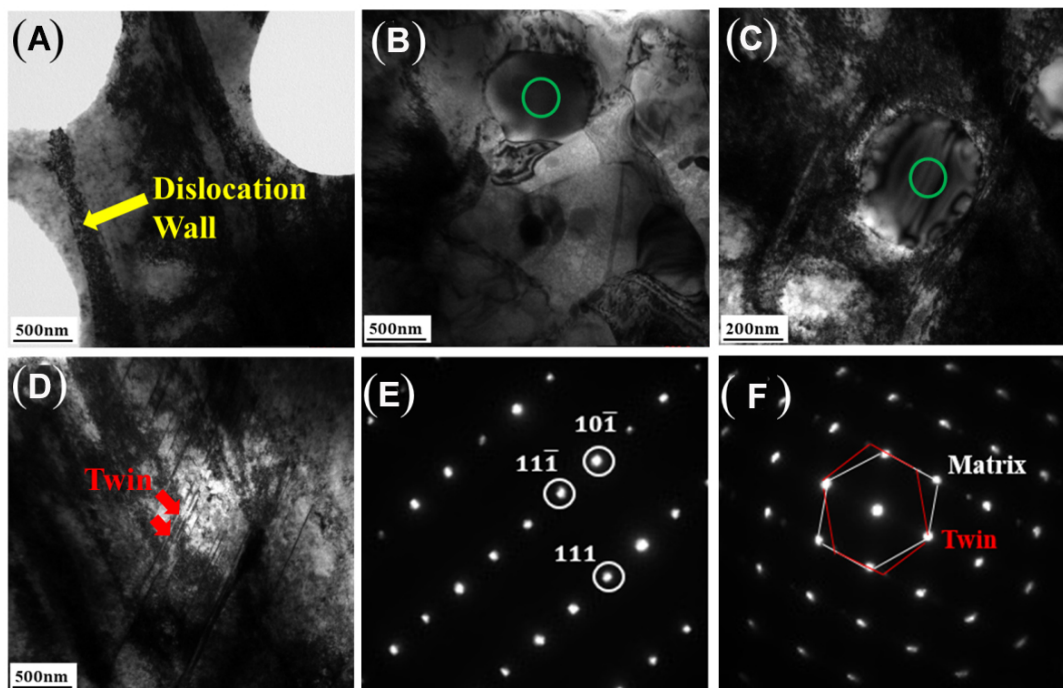


Figure 6. TEM micrograph of $\text{Fe}_{40}\text{Mn}_{20}\text{Cr}_{20}\text{Ni}_{20}$ HEA. (A) Bright-field TEM images for HEA. (B-D) TEM images of a precipitate and twins in a tensile specimen strained to fracture at 77 K. (E) SAED patterns indexed as a tetragonal-structured precipitate along the zone direction of [101]. (F) SAED pattern of the twin in (D). TEM: Transmission electron microscopy; HEA: high-entropy alloy; SAED: selective area electron diffraction.

shows the SAED pattern of the twin in Figure 6D. SEM-EDS [Figure 7] also confirmed that the precipitate is rich in Cr and poor in Fe. The combined line scans in Figure 7b are performed along the grain boundaries that intersected the Cr-rich particles. Based on the SAED and SEM-EDS analysis in Figure 7 and XRD, the structure of the Cr-rich phase can be identified.

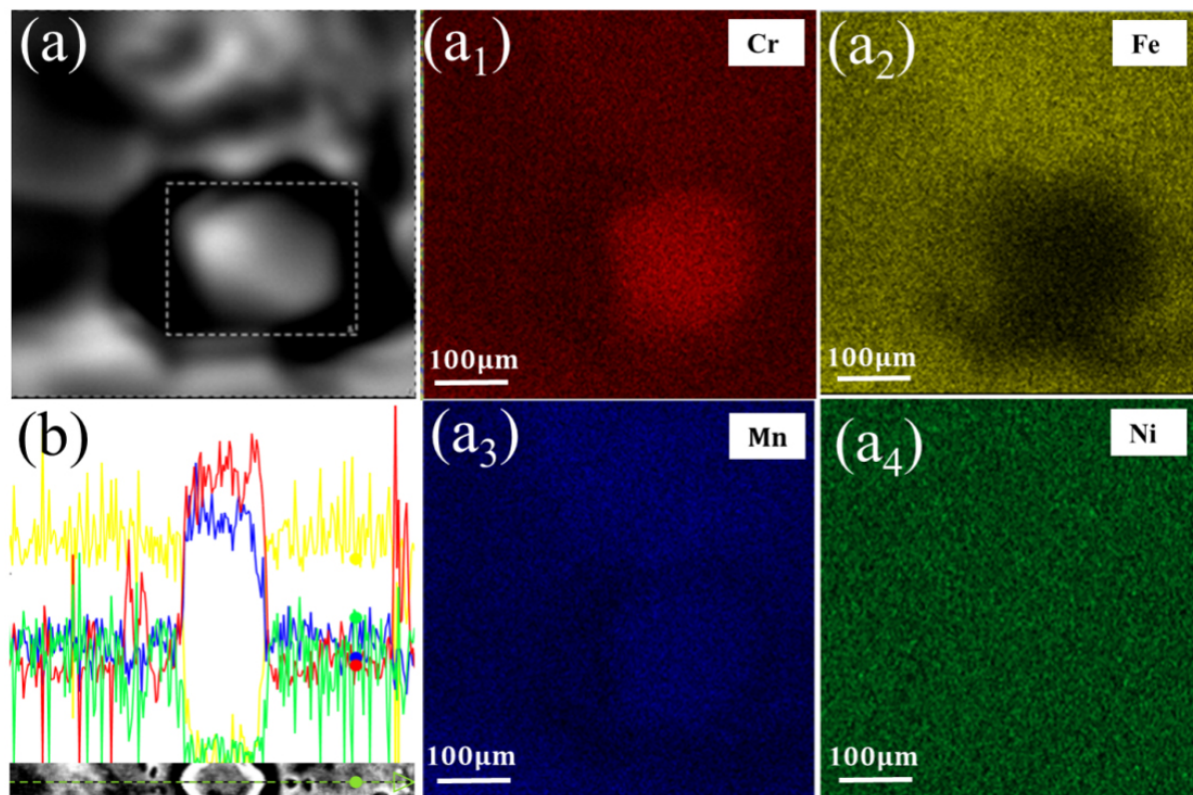


Figure 7. SEM-EDS of a precipitate phase. (a) SEM map image of precipitate and (a₁-a₄) elemental mapping results of $\text{Fe}_{40}\text{Mn}_{20}\text{Cr}_{20}\text{Ni}_{20}$ HEA for Mn, Fe, Cr and Ni, respectively. (b) Combined line scan of precipitate. HEA: High-entropy alloy.

The σ phase and its Cr content of 46.5 at.% were first reported in 1950 by Shoemaker and Bergman for the Fe-Cr system^[17]. The presented results show significant similarity to those of Schuh *et al.* where a second phase is formed after annealing at a temperature of 450 °C-750 °C^[17]. The secondary phase found in this study is the tetragonal Cr-rich σ phase, which is consistent with the phases observed in the long-term annealed alloys at 700 °C. Based on the above, they are completely confirmed as the σ stage^[16].

Mechanical properties of HEA

Representative engineering tensile stress-strain curves of the samples annealed at 600, 700, 800, and 900 °C are displayed in Figure 8A. The yield strength, fracture strength and fracture strain are exhibited in Figure 8B. As can be found in Figure 8A and B, the yield strength of the hot-rolled $\text{Fe}_{40}\text{Mn}_{20}\text{Cr}_{20}\text{Ni}_{20}$ HEA is 380 MPa, which is more than double those of $\text{Fe}-20\text{Cr}-10\text{Ni}$ ^[18], $\text{Fe}-20\text{Cr}-12\text{Ni}$ ^[19], and $\text{Fe}-16\text{Cr}-10\text{Ni}$ steels^[20]. Moreover, the elongations are also increased. After cold rolling, the yield strength increases to 920 MPa. Although the subsequent annealing at 600 °C for 2 h further strengthens the alloy, it simultaneously induces brittleness, similar to the results of Gu *et al.*^[21]. High-temperature annealing will generally soften an alloy significantly, accompanied by a decrease in yield strength but an increase in ductility. After rolling and annealing at 900 °C for 2 h, the yield strength remains unchanged and the UTS is improved from 380 to 480 MPa, while the fracture strain is increased from 30% to 43%. The yield strength of 637 MPa and the UTS of 676 MPa were achieved for the annealed sample at 700 °C, although the total elongation was reduced to 15%. Compared with the cold-rolled samples annealed at 600 and 900 °C, the alloy annealed at 800 °C suggests a good combination of high strength and ductility.

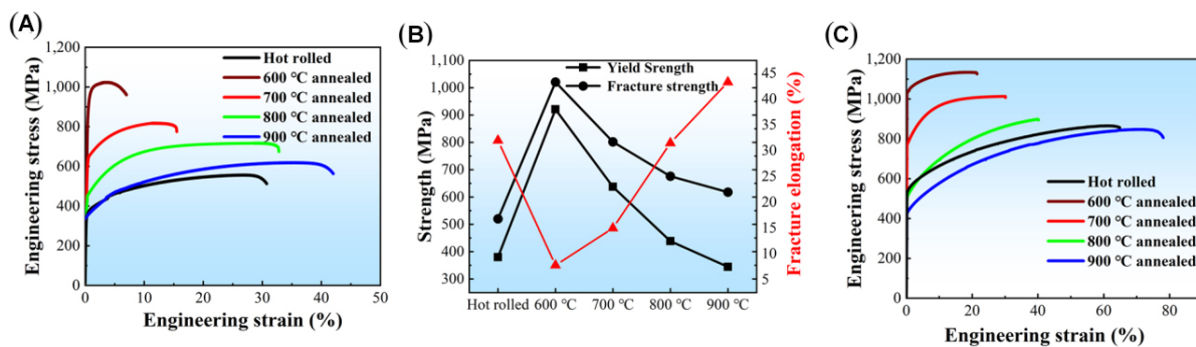


Figure 8. Mechanical properties of $\text{Fe}_{40}\text{Mn}_{20}\text{Cr}_{20}\text{Ni}_{20}$ HEA upon deformation at 298 and 77 K. (A and B) Engineering stress-strain curves, yield strength, UTS, and fracture strain at room temperature. (C) Engineering stress-strain curves upon deformation at 77 K. HEA: High-entropy alloy; UTS: ultimate tensile strength.

While the tensile ductility is remarkably increased with the decrease in the annealing temperature at 77 K, just like at room temperature, the mechanical properties of the HEA at low temperatures are obviously higher than those at room temperature [Figure 8C]. Typically, for the incompletely recrystallized alloy annealed at 700 °C, the yield strength, tensile strength, and elongation after fracture are increased by 26%, 22%, and 100%, respectively. For the completely recrystallized alloy annealed at 900 °C, the yield strength, UTS, and elongation after fracture are increased by 16%, 31%, and 86%, respectively. The HEA has good plastic deformation ability at low temperatures^[22-26]. This is because the alloy has a low stacking fault energy and a large number of deformation twins is generated during low-temperature deformation, resulting in the twinning-induced plasticity effect, which significantly improves the strength and plasticity of the alloy.

For HEAs with the FCC structure, the deformation mechanism at room temperature is dislocation slip. However, at low temperatures, due to dislocation movement becoming difficult, the strength and ductility increase simultaneously. The continuous activation of deformed twins leads to an increase in strength and ductility at low temperatures, which is attributed to the continuous activation of deformed twins^[27]. This feature is because the analytical shear stress can reach the critical stress of twins at low temperatures, resulting in highly sustained strain hardening through the dynamic Hall-Page effect. According to the results of Jo *et al.*^[28], strengthening and strain hardening have a significant influence on the σ phase. In addition, the grain size is further reduced due to grain boundary pinning. However, this has not been reported in previous studies on HEAs. This result is unexpected because it is generally believed that the presence of the σ phase formed in conventional alloys or HEAs will severely reduce the mechanical properties^[29]. Too many σ -phases particles lead to low ductility, so the most important link is to adjust the volume fraction of the σ phase. The low-temperature yield strength and elongation of the alloy in this study are compared with other FCC structural alloys, as shown in Figure 9A. Clearly, the present HEA has better low-temperature mechanical properties than those of other alloys, for example, Al alloys^[30], high Mn steels^[31], Ni-based steels^[32,33], transformation-induced plasticity steels^[34] and other HEAs^[4,23-25,35-43]. It is particularly obvious that the yield strength and UTS are the highest, with values of 1080 and 1150 MPa, annealed at 600 °C, respectively, with a loss of ductility.

Figure 9B presents the cost and elongation of samples with different annealing treatments of the current HEA at 77 K, with the results of many recently developed structural alloys also included. Compared with traditional Al alloys^[44], Mg alloys^[35,45], Ni-based steels^[46], Fe-Mn steels^[47,48], high Mn steels^[49,50], CrMn-based alloys^[51], 304 steels and even most HEAs^[4,36,37], although the strength is slightly lower than that of Ti alloys, the HEA studied has a significant cost advantage. Since there is no expensive Co element, but there is a very

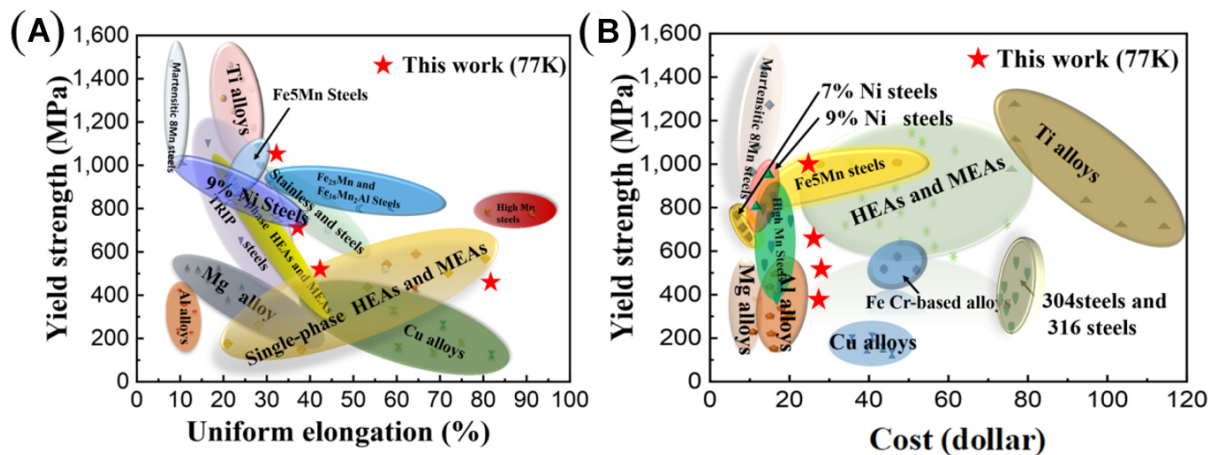


Figure 9. Comparison of yield strength versus uniform elongation and cost upon deformation at 77 K. (A) Comparison of yield strength and elongation of $\text{Fe}_{40}\text{Mn}_{20}\text{Cr}_{20}\text{Ni}_{20}$ HEA with some reported alloys. (B) Cost comparison of $\text{Fe}_{40}\text{Mn}_{20}\text{Cr}_{20}\text{Ni}_{20}$ HEA with several alloys. HEA: High-entropy alloy.

economical Fe element, the current alloy is more economical than other HEAs. This kind of alloy with excellent mechanical properties and a low cost, therefore, exhibits broad application prospects as a structural material at low temperatures and will bring new opportunities for the development of other HEAs.

Deformation mechanisms of HEA

The low-temperature mechanical properties of the HEA are much better than the room-temperature mechanical properties, which is closely related to its deformation mechanism at low temperatures. In recent years, many studies have demonstrated that FCC HEAs have low stacking fault energy at low temperatures and twins are more easily activated, thereby causing the deformation mechanism of HEAs to change from dislocation slip to dislocation slip and twinning.

In order to further study the deformation mechanism at low temperature, TEM analysis was performed near the fracture surface. Figure 6A indicates that a large number of dislocation cells were formed after tensile fracture, demonstrating that there is a high dislocation density within the crystal grains. Compared with the hot-rolled HEAs, this is the most important reason for the substantial increase in strength. During the stretching process, the mobile dislocation slides along the active slip system and may be hindered by the dislocation, geometrically necessary dislocations (GNDs), and precipitates, thus resulting in dislocation accumulation and high yield strength. Figure 6D shows a TEM image of the $\text{Fe}_{40}\text{Mn}_{20}\text{Cr}_{20}\text{Ni}_{20}$ HEA annealed at 700 °C for 2 h after low-temperature tension. Many primary twins are generated in the coarse grains that have not been recrystallized during the low-temperature deformation. The SAED pattern in Figure 6F proves the existence of deformed twins. This clearly suggests that twins are activated at 77 K. At present, it is generally believed that twins in the deformation process continuously introduce new interfaces and work hardening occurs by reducing the mean free path of dislocations. In addition, Idrissi *et al.*^[52] investigated mechanical twins with high-density dislocations, which act as an effective barrier to dislocation sliding, which further greatly promotes strain hardening. Therefore, the tensile performance of the HEA at low temperature is better than that at room temperature. Moreover, it has an enhanced work-hardening ability at low temperatures.

After annealing at 700 °C, the microstructure of the HEA is a heterogeneous structure composed of grains with different grain sizes and dislocation density distributions. Its high yield strength and relatively large plasticity are mainly owing to the multiple strengthening mechanisms of complex heterogeneous structures and high strain-hardening capabilities provided^[53], which can effectively prevent the occurrence of a stress concentration. According to a previous study^[54], since pre-existing dislocations can provide a large number of nucleation points for dislocation proliferation, non-recrystallized grains undergo plastic deformation mainly through the dislocation slip at the initial stage of deformation. As the strain increases, dislocation slip is largely activated in non-recrystallized grains, while dislocation slip in most recrystallized grains is greatly restricted. Therefore, the dislocations in the non-recrystallized grains gather around the grain boundaries of the recrystallized grains instead of inside the grains.

In addition, due to the difference in the internal plastic strains of the two kinds of grains, the strain incompatibility at the grain boundaries between the non-recrystallized and recrystallized grains is continuously enhanced. Therefore, GNDs are required to maintain the continuity of strains. Simultaneously, the newly proliferated dislocations inside the non-recrystallized grains interact with the original dislocations, leading to the annihilation of the dislocations, and the dislocation density is greatly reduced. As the strain increases, the twins in the non-recrystallized grains can be continuously activated, thereby further increasing the strain-hardening rate.

The activation of twins in non-recrystallized grains indicates that dislocations can accumulate at the interface of deformed twins, resulting in increased incompatibility within non-recrystallized grains, and this incompatibility will also increase the back stress^[55]. The dislocation density in the non-recrystallized grains increases and the degree of dislocation strengthening is more obvious. Therefore, back-stress strengthening and dislocation strengthening promote strain hardening. More dislocations are activated at the grain boundaries and the back stress is significantly reduced. Furthermore, the dislocation source is largely activated at the recrystallized grain boundaries. Therefore, the dislocation density in the recrystallized grains is significantly increased. As a result, the twins in the recrystallized grains are activated, thereby gradually increasing the strain-hardening rate. The dislocation nucleation points between the non-recrystallized and recrystallized grains increase and the internal dislocation sources of the recrystallized grains increase, which activates the deformation mechanism of the plasticity dominated by the dislocation slips. As the flow stress increases, more twins in the heterogeneous structure are activated, resulting in an increase in the twin density and twin thickness and a decrease in twin spacing. The dense twin substructure can hinder the formation of dislocations and further enhance the dislocation hardening ability.

Here, a more detailed and intuitive understanding of the deformation mechanisms of the incomplete and complete recrystallization is urgently needed. [Figure 10](#) shows a schematic of the deformation process in the partially recrystallized alloy at 700 °C annealing and fully recrystallized specimen at 900 °C annealing. It can be seen that before tensile deformation, the grain size of recrystallization at 700 °C is much smaller than that at 900 °C, but the precipitate size is larger than that at 900 °C. Part of the precipitated phase of recrystallization is mainly distributed at the triple points and grain boundaries, and a small amount is distributed in the grain interior. However, the precipitated phase of the complete recrystallization is more distributed within the grain. Moreover, the size of the precipitated phase distributed at the triple points and grain boundaries is obviously larger than that in the grain [[Figure 4](#)]. After tensile deformation, a large number of dislocations and twins appeared in both partially and fully recrystallized structures, while no twins were observed in fine grains partially recrystallized at 700 °C. The deformation twins were mainly distributed in coarse grains that were not recrystallized. This trend can be explained by the different magnitudes of twin critical stresses in different regions.

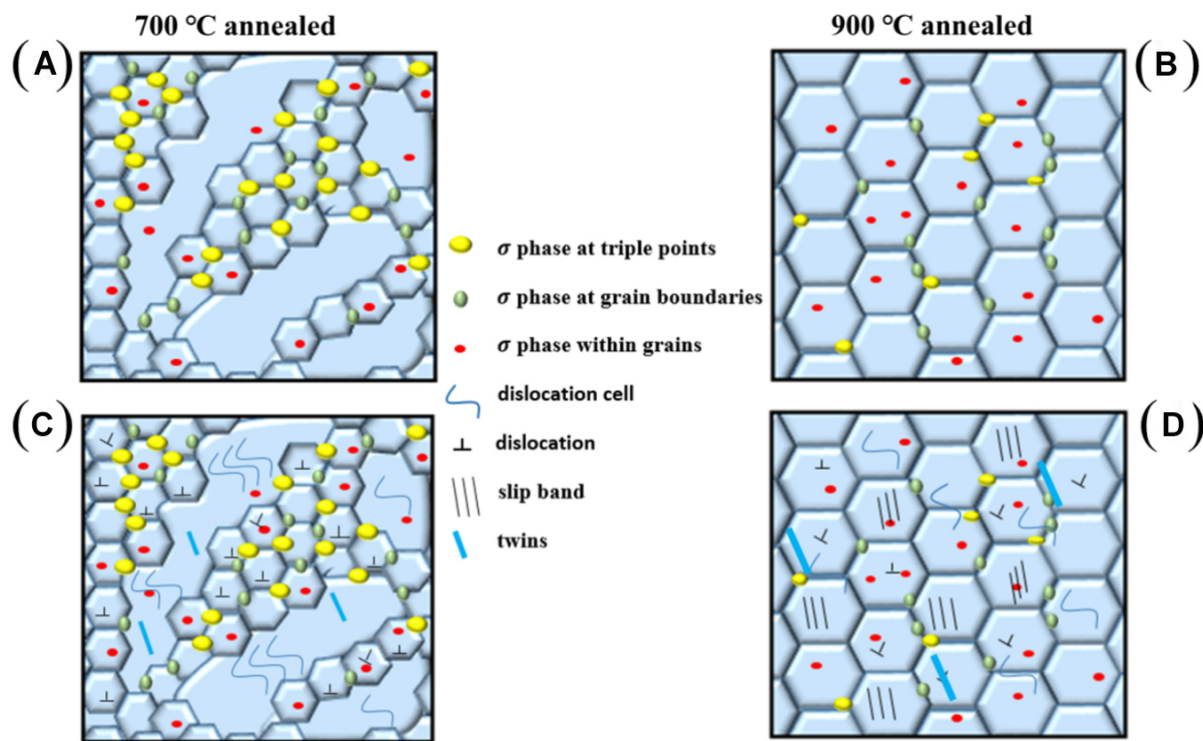


Figure 10. Tensile deformation process of HEA annealed at 700 and 900 °C for 2 h. (A and B) Schematics of the microstructure of non-deformed sample. (C and D) Schematics of the microstructure of sample after fracture. HEA: High-entropy alloy.

However, various microstructures of incompletely recrystallized $\text{Fe}_{40}\text{Mn}_{20}\text{Cr}_{20}\text{Ni}_{20}$ HEAs have different deformation modes under low-temperature tension. The deformation modes of the non-recrystallized coarse grains are dislocation slip and twinning, while the deformation mode of the recrystallized fine grain is dislocation slip.

Compared with the hot-rolled HEA, this characteristic is the main cause of significant strengthening. When the HEA is annealed at 700 °C, there is a heterogeneous structure of grains with two different length scales and dislocation density inhomogeneity. At 77 K, the relatively high yield and ductility are attributable to the excellent strain hardening ability caused by the multiple strengthening mechanisms of the complex heterogeneous structure, which can avoid strain localization. Usually, the plastic deformation of non-recrystallized grains is mainly caused by dislocation slip at the beginning of deformation, which leads to dislocation and GND accumulation around grain boundaries. Further strain causes the twins in the non-recrystallized grains to be activated. The back-stress hardening and twins in the non-recrystallized grains increase the rate of strain hardening through strain. Some of the recrystallized grains surrounding the non-recrystallized grains undergo plastic deformation by strained dislocation slip. Although most of the recrystallized grains are deformed by dislocation slip, the twinning can still be activated, which significantly increases the rate of strain hardening. Increasingly more twins can be activated in non-recrystallized and recrystallized grains through strain. Dislocation sliding is highly activated in these grains and is propagated through the grain boundaries.

Therefore, the increase in the effective stress has the same effect as the decrease in the back stress, resulting in a more uniform distribution of dislocations within and between grains. In short, this special deformation mechanism enables the heterogeneous structures to continuously undergo uniform elongation. It is

precisely due to this special heterogeneous structure that the multicomponent HEA exhibits excellent comprehensive mechanical properties at low temperatures.

Compared with high-temperature annealing, the alloy annealed at 700 °C for 2 h has an incomplete recrystallization structure, which has a higher yield strength. In order to study the yield strengths of alloys with different strengthening methods, different strengthening mechanisms were quantitatively analyzed. Generally, the strengthening mechanisms of alloys include grain boundary, dislocation, and precipitation strengthening. The yield strength of the current HEAs can be calculated by^[56]:

$$\sigma_y = \sigma_0 + \Delta\sigma_g + \Delta\sigma_d + \Delta\sigma_p \quad (1)$$

where σ_0 is the initial yield strength of the homogeneous alloy and $\Delta\sigma_g$, $\Delta\sigma_d$, and $\Delta\sigma_p$ are grain boundary, dislocation, and precipitation strengthening, respectively.

It is well known that this contribution of the refined grains to the yield strengths of alloys can be calculated using the classical Hall-Petch relation^[57]:

$$\Delta\sigma_g = k_t(d^{-1/2} - d_0^{-1/2}) \quad (2)$$

where d and d_0 are the average grain sizes of the alloy and hot-rolled alloy, respectively, and k_t represents the grain boundary strengthening coefficient (494 MPa · $\sqrt{\mu m}$)^[4]. According to Eq. (2), the contribution of grain boundary strengthening to the yield strength of the incompletely recrystallized alloy is ~144 MPa. For the alloy annealed at 900 °C, the grain boundary strengthening value is 34.5 MPa. $\Delta\sigma_d$ is the increase in the strength due to dislocations. Therefore, it can be considered, employing the Taylor-hardening law^[58]:

$$\Delta\sigma_d = M\alpha G b \rho_d^{1/2} \quad (3)$$

where M represents the Taylor factor (3.06) that converts shear stress to normal stress, α is a constant (0.26), G is the shear modulus estimated as 85 GPa for this HEA^[59] and ρ is the dislocation density, which was estimated to be $\sim 10^{12} \text{ m}^{-2}$. The estimates of the dislocation density from the EBSD and XRD analysis are of the same order of magnitude. The value of the dislocation hardening ($\Delta\sigma_d$) is 297 MPa. For the recrystallized alloy annealed at 900 °C, the dislocation density inside the grain is very small^[60].

It is generally accepted that there are two different mechanisms of precipitation strengthening, namely, the Orowan looping mechanism and the dislocation shearing mechanism. The grain morphology distribution is the main factor affecting alloy strength, including grain size, shape, and spacing. When the particle radius is larger than the critical value or the particle is not coherent with the matrix, the Orowan mechanism is usually dominant. In contrast, when the precipitates are very small and coherent, a shearing mechanism occurs. The precipitation strengthening in this study is considered to be mainly due to the Orowan mechanism. Therefore, the contribution of precipitates is given as^[61]:

$$\Delta\sigma_p = 0.538 \times \frac{Gb f_p^{0.5}}{D_p} \ln \left(\frac{D_p}{2b} \right) \quad (4)$$

where G is the shear modulus of the matrix, 85 GPa, for the studied alloy, which is measured by the frequency at room temperature, b is the Burgers vector (0.255 nm), and D_p and f_o are the average grain size and phase fraction of the precipitates (the specific values are listed in [Table 2](#)), respectively. The calculated incremental contributions of 700 °C for 2 h and 900 °C for 2 h samples from precipitation strengthening are 14.2 and 66.5 MPa, respectively.

In summary, the calculated yield strength of the incompletely recrystallized alloy annealed at 700 °C for 2 h is 665 MPa, which is in good agreement with the experimental result of ~640 MPa. The yield strength of the recrystallized alloy at 900 °C is 320 MPa, which is close to the result from the experiments of 334 MPa. The calculated errors are 3.9% and 4.1% for the alloys annealed at 700 and 900 °C, respectively, and may be due to the following reasons. Firstly, the alloy contains a small amount of annealing twins and stacking faults, which hinder the movement of dislocations, thereby increasing the strength of the alloy. Secondly, to simplify the calculation, the precipitate particles are regarded as spherical particles in this study; however, the alloy also contains a small amount of irregular tabular or square precipitates. Irregular plate-like or square precipitates are more capable of hindering dislocation motion than spherical precipitates, so the calculation process underestimates the contribution of precipitation strengthening to yield strength.

Recrystallization kinetics of HEA

In this study, the recrystallization behavior of the HEA was quantitatively studied using the JMAK model^[12]:

$$X = 1 - \exp(-Bt^n) \quad (5)$$

where X represents the recrystallized fraction given by the surface area fraction of the alloy (%), t is the annealed time at the given temperature, B is a rate constant, and n is a temperature-independent index related to the nucleation and growth rates, density and distribution of nucleation sites.

[Figure 11A](#) presents $\log[\ln(1/(1-X))]$ as a function of $\log[ln(t)]$ to calculate the Avrami constant, n . It can be seen that the Avrami diagram in [Figure 11B](#) is approximately linear and the n value obtained varies between 0.56 at 600 °C and 0.75 at 700 °C. It is reported that these values of most materials, which are associated with recrystallization, are 1-2, and the deformation variables normally make no difference at that time^[31]. However, some studies report that this n value can be affected by the temperature and initial grain size. As the temperature decreases or the grain size increases, the n has a fixed value of 1, which is unrelated to the deformation variables. In the current work, the grain sizes of the 600, 700, and 800 °C annealed samples are 3.2, 5.4, and 8.5 μm, respectively. These grain sizes are much smaller than 50 μm. The n value studied by Lü et al. increases with increasing temperature from 0.70 at 560 °C to 0.90 at 670 °C^[62]. The value of n in the current study is also maintained in the range of 0.5-1.0, as reported by Lü et al.^[62]. However, these results are still not well understood for different values of n .

The variation trend of the recrystallized fraction of the Fe₄₀Mn₂₀Cr₂₀Ni₂₀ HEA with annealing time and temperature is presented in [Figure 11B](#). After the steady-state stage, the recrystallized rate gradually increases up to the 50% recrystallized fraction (midpoint), after which the rate decreases and stops at an almost fully recrystallized fraction (~98%). According to the traditional definition of the recrystallization temperature (the minimum temperature at which the recrystallization (greater than the 95% transition) can be completed within the 1 h holding time for the cold-deformed metal with large deformation (greater than 70%)^[12], the recrystallized temperature of the cold-rolled Fe₄₀Mn₂₀Cr₂₀Ni₂₀ is ~800 °C.

Table 2. Important parameters affecting mechanical properties of studied materials

	FCC phase		σ phase	
	Grain size (nm)	Phase fraction (%)	Diameter (nm)	Phase fraction (%)
700 °C annealed	3120	81.8	1438	18.2
900 °C annealed	8450	89.6	734.7	10.4

FCC: Face-centered-cubic.

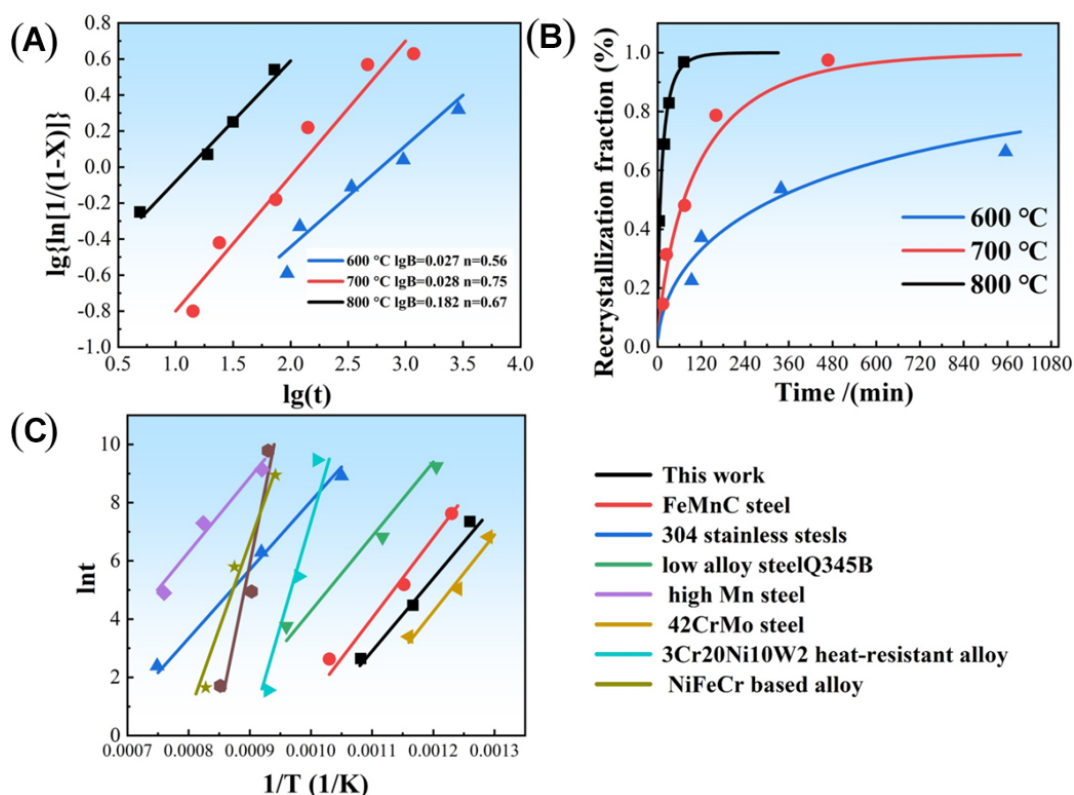


Figure 11. Recrystallization kinetics of $\text{Fe}_{40}\text{Mn}_{20}\text{Cr}_{20}\text{Ni}_{20}$ HEA. (A) JMAK plots. (B) Recrystallized fraction against time plots. (C) Recrystallization activation energy of $\text{Fe}_{40}\text{Mn}_{20}\text{Cr}_{20}\text{Ni}_{20}$ and other reported alloys, including FeMnC steels, 304 stainless steels, low alloy steel Q345B, high Mn steel, 42CrMo steel, and 3Cr20Ni10W2 heat-resistant and NiFeCr-based alloys. HEA: high-entropy alloy.

To further study the difference in temperature and time of the recrystallization kinetics of different HEAs, we adopt an Arrhenius-type relationship to study the activation energy of recrystallization^[12].

$$\frac{1}{t} = A \exp\left(-\frac{Q}{RT}\right) \quad (6)$$

where t is the characteristic recrystallization time corresponding to the recrystallization volume (the fixed value we use here is 50%, which is $t_{0.5}$), R is the universal gas constant, T is the deformation annealed temperature, Q is the apparent activation energy of recrystallization (kJ/mol), and A is the pre-exponential factor. Static recrystallization is one of the thermally-activated processes. Hence, the activation energy can be obtained from Figure 11C. The time for 50% softening has a linear relationship with temperature, and Q can be extracted from the slopes of the curves in Figure 11C as 207 kJ/mol. The value is less than the activation energy of self-diffusion in γ -Fe (270 kJ/mol).

We also compared the activation energy of FeMnC steels^[63], 304 stainless steels^[64], Q345B high-alloy steels^[65], 42CrMo steels^[66], 3Cr20Ni10W2 steels^[67] and NiFeCr-based alloys^[68]. This value is significantly smaller than that for dynamic recrystallization (380 kJ/mol), meaning that the temperature dependency for static recrystallization is lower than that of dynamic recrystallization. In the case of stainless steels, there are many studies regarding static recrystallization kinetics. It is known that the activation energy of the static recrystallization of microalloyed steels is 240 kJ/mol. According to the study of Yang *et al.*, the compositional difference of HEAs mainly affects the recrystallization kinetics^[60]. The extrapolated recrystallization activation energy is opposite to the diffusion activation energy, indicating that the volume diffusion cannot control the recrystallization process of the alloy. The studied HEA activation energy of recrystallization is not significantly different from that of a Fe-Mn-C steel or a Ni-Fe-Cr alloy. They have a similar stacking fault energy, just like most single-phase FCC HEAs^[68]. The extruded Q value of the 3Cr20Ni10W2 alloy calculated by Quan *et al.* is 892.4 kJ/mol^[67], which is significantly greater than that of the studied HEA. Generally, the activation energy during thermal deformation is a function of various parameters, such as the chemical alloy-type elemental composition, initial microstructure, and test conditions.

In addition, deformation twins hinder the movement of dislocations, thereby increasing the energy-driven recrystallization. According to the Bailey-Hirsch relationship^[69], the strain-hardening capacity is proportional to the square root of the dislocation density. Hence, it is reasonable to assume that the greater the strain hardening, the higher the dislocation density. For example, twin boundaries and the introduction of twins were found in α -titanium^[70] to improve the microstructure inhomogeneity, leading to the promoted static recrystallization process. In addition, more nucleation sites are found in the shear bands, grain boundaries, and tri-junctions of Fe-Mn-C steels^[63], which are inhomogeneous with the local orientation gradient.

CONCLUSIONS

The current research work discusses the microstructure and mechanical properties of hot- and cold-rolled $\text{Fe}_{40}\text{Mn}_{20}\text{Cr}_{20}\text{Ni}_{20}$ HEAs annealed at different temperatures. The material was cold-rolled and annealed in a temperature range from 600 °C-900 °C for 2 h at room temperature and 77 K. The second phases, enriched in Cr, were observed. The mechanical properties of the current HEA at low temperature were better than that at room temperature. We mainly studied the deformation mechanism without partially recrystallized annealing at 700 °C and completely recrystallized annealing at 900 °C. The static recrystallization kinetics in the cold-rolled $\text{Fe}_{40}\text{Mn}_{20}\text{Cr}_{20}\text{Ni}_{20}$ HEAs were experimentally characterized with annealing at 600 and 800 °C. The following conclusions can be drawn:

- (1) The alloy exhibited a partially recrystallized structure when cold rolled and annealed at 700 °C. It was composed of fine grains that were not completely recrystallized, which contained high-density dislocations. When the annealing temperature was 900 °C, a completely recrystallized structure was formed and the grain size increased simultaneously.
- (2) The $\text{Fe}_{40}\text{Mn}_{20}\text{Cr}_{20}\text{Ni}_{20}$ HEA had a yield strength of 800 MPa and a good elongation (30%) after an 82% thickness reduction and annealing at 700 °C. This feature was not only related to dislocation strengthening but also depended on the strengthening effect of deformed twins.
- (3) The JMAK model was in good agreement with the recrystallization kinetics curves of the $\text{Fe}_{40}\text{Mn}_{20}\text{Cr}_{20}\text{Ni}_{20}$ HEAs. The Avrami index of $\text{Fe}_{40}\text{Mn}_{20}\text{Cr}_{20}\text{Ni}_{20}$ HEA at 82% cold-rolled deformation and 600 °C annealing temperature fluctuates between 0.56 and 0.75. The Arrhenius law with an apparent activation

energy of 207 kJ/mol can describe the temperature dependence of recrystallization kinetics well. This value is consistent with the diffusion value of the grain boundaries, and its ratio to the diffusion value of Cr and Ni is 3:2.

DECLARATIONS

Acknowledgments

The authors would like to acknowledge the financial support of the Key Research and Development Program of Shanxi Province (No. 202102050201008). PKL appreciates support from (1) the National Science Foundation (DMR-1611180 and 1809640) with program directors, Drs. Yang J, Shiflet G, and Farkas D and (2) the US Army Research Office (W911NF-13-1-0438 and W911NF-19-20049) with program managers, Drs. Bakas MP, Mathaudhu SN and Stepp DM.

Authors' contributions

Writing: Ma QX

Methodology: Yang HJ

Figures and study design: Wang Z

Data collection: Shi XH

Data analysis: Liaw PK

Data interpretation and validation: Qiao JW

All authors have read and agreed to the published version of the manuscript.

Availability of data and materials

The data that support the findings of this study are available from the corresponding author upon reasonable request.

Financial support and sponsorship

This work was supported by the Key Research and Development Program of Shanxi Province (No. 202102050201008). PKL appreciates support from (1) the National Science Foundation (DMR-1611180 and 1809640) with program directors, Drs. Yang J, Shiflet G, and Farkas D and (2) the US Army Research Office (W911NF-13-1-0438 and W911NF-19-20049) with program managers, Drs. Bakas MP, Mathaudhu SN, and Stepp DM.

Conflicts of interest

All authors declared that there are no conflicts of interest.

Ethical approval and consent to participate

Not applicable.

Consent for publication

Not applicable.

Copyright

© The Author(s) 2022.

REFERENCES

- Li Z, Pradeep KG, Deng Y, Raabe D, Tasan CC. Metastable high-entropy dual-phase alloys overcome the strength-ductility trade-off. *Nature* 2016;534:227-30. [DOI](#) [PubMed](#)
- Zhang Z, Sheng H, Wang Z, et al. Dislocation mechanisms and 3D twin architectures generate exceptional strength-ductility-toughness combination in CrCoNi medium-entropy alloy. *Nat Commun* 2017;8:14390. [DOI](#) [PubMed](#) [PMC](#)

3. Jo YH, Jung S, Choi WM, et al. Cryogenic strength improvement by utilizing room-temperature deformation twinning in a partially recrystallized VCrMnFeCoNi high-entropy alloy. *Nat Commun* 2017;8:15719. [DOI](#) [PubMed](#) [PMC](#)
4. Otto F, Dlouhý A, Somsen C, Bei H, Eggeler G, George E. The influences of temperature and microstructure on the tensile properties of a CoCrFeMnNi high-entropy alloy. *Acta Materialia* 2013;61:5743-55. [DOI](#)
5. Rao J, Diao H, Ocelík V, et al. Secondary phases in Al_xCoCrFeNi high-entropy alloys: an in-situ TEM heating study and thermodynamic appraisal. *Acta Materialia* 2017;131:206-20. [DOI](#)
6. Yeh J. Alloy design strategies and future trends in high-entropy alloys. *JOM* 2013;65:1759-71. [DOI](#)
7. Yeh J, Chang S, Hong Y, Chen S, Lin S. Anomalous decrease in X-ray diffraction intensities of Cu-Ni-Al-Co-Cr-Fe-Si alloy systems with multi-principal elements. *Mater Chem Phys* 2007;103:41-6. [DOI](#)
8. Lee C, Chou Y, Kim G, et al. Lattice-distortion-enhanced yield strength in a refractory high-entropy alloy. *Adv Mater* 2020;32:e2004029. [DOI](#) [PubMed](#)
9. Lee C, Song G, Gao MC, et al. Lattice distortion in a strong and ductile refractory high-entropy alloy. *Acta Materialia* 2018;160:158-72. [DOI](#)
10. Tsai K, Tsai M, Yeh J. Sluggish diffusion in Co-Cr-Fe-Mn-Ni high-entropy alloys. *Acta Materialia* 2013;61:4887-97. [DOI](#)
11. Sohn SS, Kwiatkowski da Silva A, Ikeda Y, et al. Ultrastrong medium-entropy single-phase alloys designed via severe lattice distortion. *Adv Mater* 2019;31:e1807142. [DOI](#) [PubMed](#)
12. Rollett A, Humphreys F, Rohrer GS, Hatherly M. Recrystallization and related annealing phenomena: second edition, recrystallization and related annealing phenomena, 2nd edition, 2004; pp. 1-628. Available from: <https://www.elsevier.com/books/recrystallization-and-related-annealing-phenomena/rollett/978-0-08-044164-1> [Last accessed on 19 July 2022].
13. Lee CP. Boundary negotiating artifacts: unbinding the routine of boundary objects and embracing chaos in collaborative work. *Comput Supported Coop Work* 2007;16:307-39. [DOI](#)
14. Shi Y, Yang B, Liaw P. Corrosion-resistant high-entropy alloys: a review. *Metals* 2017;7:43. [DOI](#)
15. Shi Y, Yang B, Xie X, Brechtl J, Dahmen KA, Liaw PK. Corrosion of Al CoCrFeNi high-entropy alloys: Al-content and potential scan-rate dependent pitting behavior. *Corros Sci* 2017;119:33-45. [DOI](#)
16. Laplanche G, Berglund S, Reinhart C, Kostka A, Fox F, George E. Phase stability and kinetics of σ-phase precipitation in CrMnFeCoNi high-entropy alloys. *Acta Materialia* 2018;161:338-51. [DOI](#)
17. Schuh B, Mendez-Martin F, Volker B, et al. Mechanical properties, microstructure and thermal stability of a nanocrystalline CoCrFeMnNi high-entropy alloy after severe plastic deformation. *Acta Mater* 2015;96:258-268. [DOI](#)
18. Li S, Wang Y, Wang X. Effects of Ni content on the microstructures, mechanical properties and thermal aging embrittlement behaviors of Fe-20Cr-xNi alloys. *Mater Sci Eng A* 2015;639:640-6. [DOI](#)
19. Oh K, Ahn S, Eom K, Kwon H. A study on the localized corrosion and repassivation kinetics of Fe-20Cr- x Ni (x = 0-20 wt%) stainless steels via electrochemical analysis. *Corros Sci* 2015;100:158-68. [DOI](#)
20. Misra R, Zhang Z, Venkatasurya P, Somani M, Karjalainen L. Martensite shear phase reversion-induced nanograined/ultrafine-grained Fe-16Cr-10Ni alloy: the effect of interstitial alloying elements and degree of austenite stability on phase reversion. *Mater Sci Eng A* 2010;527:7779-92. [DOI](#)
21. Gu J, Song M. Annealing-induced abnormal hardening in a cold rolled CrMnFeCoNi high entropy alloy. *Scripta Materialia* 2019;162:345-9. [DOI](#)
22. Moon J, Tabachnikova E, Shumilin S, et al. Deformation behavior of a Co-Cr-Fe-Ni-Mo medium-entropy alloy at extremely low temperatures. *Mater Today* 2021;50:55-68. [DOI](#)
23. Bian B, Guo N, Yang H, et al. A novel cobalt-free FeMnCrNi medium-entropy alloy with exceptional yield strength and ductility at cryogenic temperature. *J Alloys Comp* 2020;827:153981. [DOI](#)
24. Li D, Li C, Feng T, et al. High-entropy Al0.3CoCrFeNi alloy fibers with high tensile strength and ductility at ambient and cryogenic temperatures. *Acta Materialia* 2017;123:285-94. [DOI](#)
25. Tasan CC, Deng Y, Pradeep KG, Yao MJ, Springer H, Raabe D. Composition Dependence of Phase Stability, Deformation Mechanisms, and Mechanical Properties of the CoCrFeMnNi High-Entropy Alloy System. *JOM* 2014;66:1993-2001. [DOI](#)
26. Yang J, Qiao J, Ma S, Wu G, Zhao D, Wang Z. Revealing the hall-petch relationship of Al0.1CoCrFeNi high-entropy alloy and its deformation mechanisms. *J Alloys Comp* 2019;795:269-74. [DOI](#)
27. Edalati K, Cubero-sesin JM, Alhamidi A, Mohamed IF, Horita Z. Influence of severe plastic deformation at cryogenic temperature on grain refinement and softening of pure metals: Investigation using high-pressure torsion. *Mater Sci Eng A* 2014;613:103-10. [DOI](#)
28. Jo Y, Choi W, Kim D, et al. Utilization of brittle σ phase for strengthening and strain hardening in ductile VCrFeNi high-entropy alloy. *Mater Sci Eng A* 2019;743:665-74. [DOI](#)
29. Pickering E, Muñoz-moreno R, Stone H, Jones N. Precipitation in the equiatomic high-entropy alloy CrMnFeCoNi. *Scripta Materialia* 2016;113:106-9. [DOI](#)
30. Nayan N, Narayana Murty S, Jha AK, et al. Mechanical properties of aluminium-copper-lithium alloy AA2195 at cryogenic temperatures. *Mater Des* 2014;58:445-50. [DOI](#)
31. Sohn SS, Hong S, Lee J, et al. Effects of Mn and Al contents on cryogenic-temperature tensile and Charpy impact properties in four austenitic high-Mn steels. *Acta Materialia* 2015;100:39-52. [DOI](#)
32. Cao H, Luo X, Zhan G, Liu S. Effect of intercritical quenching on the microstructure and cryogenic mechanical properties of a 7 Pct Ni steel. *Metall Mat Trans A* 2017;48:4403-10. [DOI](#)

33. Grill D, Stotter C, Sommitsch C, et al. Microstructure modeling of the dynamic recrystallization kinetics during turbine disc forging of the nickel based superalloy allvac 718 plus. 2008. [DOI](#)
34. Zhang T, Hu J, Wang C, et al. Effects of deep cryogenic treatment on the microstructure and mechanical properties of an ultrahigh-strength TRIP-aided bainitic steel. *Mater Charact* 2021;178:111247. [DOI](#)
35. Dieringa H. Influence of cryogenic temperatures on the microstructure and mechanical properties of magnesium alloys: a review. *Metals* 2017;7:38. [DOI](#)
36. Jo YH, Choi W, Sohn SS, Kim HS, Lee B, Lee S. Role of brittle sigma phase in cryogenic-temperature-strength improvement of non-equiautomatic Fe-rich VCrMnFeCoNi high entropy alloys. *Mater Sci Eng A* 2018;724:403-10. [DOI](#)
37. Jo Y, Kim D, Jo M, et al. Effects of deformation-induced BCC martensitic transformation and twinning on impact toughness and dynamic tensile response in metastable VCrFeCoNi high-entropy alloy. *J Alloys Comp* 2019;785:1056-67. [DOI](#)
38. Wu S, Wang G, Wang Q, et al. Enhancement of strength-ductility trade-off in a high-entropy alloy through a heterogeneous structure. *Acta Materialia* 2019;165:444-58. [DOI](#)
39. Yao M, Pradeep K, Tasan C, Raabe D. A novel, single phase, non-equiautomatic FeMnNiCoCr high-entropy alloy with exceptional phase stability and tensile ductility. *Scripta Materialia* 2014;72-73:5-8. [DOI](#)
40. Gludovatz B, Hohenwarter A, Thurston KV, et al. Exceptional damage-tolerance of a medium-entropy alloy CrCoNi at cryogenic temperatures. *Nat Commun* 2016;7:10602. [DOI](#) [PubMed](#) [PMC](#)
41. Qiao JW, Ma S, Huang E, Chuang C, Liaw P, Zhang Y. Microstructural characteristics and mechanical behaviors of AlCoCrFeNi high-entropy alloys at ambient and cryogenic temperatures. *MSF* 2011;688:419-25. [DOI](#)
42. Wei R, Zhang K, Chen L, et al. Novel Co-free high performance TRIP and TWIP medium-entropy alloys at cryogenic temperatures. *J Mater Sci Technol* 2020;57:153-8. [DOI](#)
43. Zherebtsov S, Stepanov N, Ivanisenko Y, et al. Evolution of microstructure and mechanical properties of a CoCrFeMnNi high-entropy alloy during high-pressure torsion at room and cryogenic temperatures. *Metals* 2018;8:123. [DOI](#)
44. Geng R, Tian W, Zhao Q, Qiu F, Jiang Q. Superior Cryogenic tensile strength and ductility of in situ Al-Cu matrix composite reinforced with 0.3 wt% Nano-Sized TiCp. *Adv Eng Mater* 2018;20:1701137. [DOI](#)
45. Zhang X, Wu G, Liu W, Ding W. Low temperature mechanical properties of as-extruded Mg-10Gd-3Y-0.5Zr magnesium alloy. *Transact Nonferr Metals Soc China* 2012;22:2883-90. [DOI](#)
46. Cao H, Luo X, Zhan G, Liu S. Effect of Mn content on microstructure and cryogenic mechanical properties of a 7% Ni steel. *Acta Metall Sin (Engl Lett)* 2018;31:699-705. [DOI](#)
47. Jeong D, Sung H, Park T, Lee J, Kim S. Fatigue crack propagation behavior of Fe₂₅Mn and Fe₁₆Mn₂Al steels at room and cryogenic temperatures. *Met Mater Int* 2016;22:601-8. [DOI](#)
48. Kwon K, Yi I, Ha Y, et al. Origin of intergranular fracture in martensitic 8Mn steel at cryogenic temperatures. *Scripta Materialia* 2013;69:420-3. [DOI](#)
49. Chen J, Ren J, Liu Z, Wang G. Interpretation of significant decrease in cryogenic-temperature Charpy impact toughness in a high manganese steel. *Mater Sci Eng A* 2018;737:158-65. [DOI](#)
50. Park J, Lee K, Sung H, Kim YJ, Kim SK, Kim S. J-integral fracture toughness of high-Mn steels at room and cryogenic temperatures. *Metall and Mat Trans A* 2019;50:2678-89. [DOI](#)
51. Astafurova EG, Moskvina VA, Maier GG, et al. Low-temperature tensile ductility by V-alloying of high-nitrogen CrMn and CrNiMn steels: characterization of deformation microstructure and fracture micromechanisms. *Mater Sci Eng A* 2019;745:265-78. [DOI](#)
52. Idrissi H, Renard K, Schryvers D, Jacques P. On the relationship between the twin internal structure and the work-hardening rate of TWIP steels. *Scripta Materialia* 2010;63:961-4. [DOI](#)
53. Komarasamy M, Kumar N, Tang Z, Mishra R, Liaw P. Effect of microstructure on the deformation mechanism of friction stir-processed Al_{0.1} CoCrFeNi high entropy alloy. *Mater Res Lett* 2015;3:30-4. [DOI](#)
54. Ghoncheh M, Sengupta J, Wu N, Gao J, Phillion A. On the hot embrittlement of continuously-cast and transfer-bar structures in DP600 advanced high-strength steel. *J Mater Proc Technol* 2021;289:116936. [DOI](#)
55. Liu X, Xue Q, Wang W, et al. Back-stress-induced strengthening and strain hardening in dual-phase steel. *Materialia* 2019;7:100376. [DOI](#)
56. Liang YJ, Wang L, Wen Y, et al. High-content ductile coherent nanoprecipitates achieve ultrastrong high-entropy alloys. *Nat Commun* 2018;9:4063. [DOI](#) [PubMed](#) [PMC](#)
57. Tao K, Choo H, Li H, Clausen B, Jin J, Lee Y. Transformation-induced plasticity in an ultrafine-grained steel: an in situ neutron diffraction study. *Appl Phys Lett* 2007;90:101911. [DOI](#)
58. Lu W, Liebscher CH, Yan F, et al. Interfacial nanophases stabilize nanotwins in high-entropy alloys. *Acta Materialia* 2020;185:218-32. [DOI](#)
59. Guo N, Zhao Y, Long S, et al. Microstructure and mechanical properties of (CrCoNi)₉₇Al_{1.5}Ti_{1.5} medium entropy alloy twisted by free-end-torsion at room and cryogenic temperatures. *Mater Sci Eng A* 2020;797:140101. [DOI](#) [PubMed](#) [PMC](#)
60. Yang Z, He F, Wu Q, et al. Distinct recrystallization kinetics in Ni-Co-Cr-Fe-based single-phase high-entropy alloys. *Metall Mater Trans A* 2021;52:3799-810. [DOI](#)
61. Gladman T. Precipitation hardening in metals. *Mater Sci Technol* 1999;15:30-6. [PubMed](#)
62. Lü Y, Molodov DA, Gottstein G. Recrystallization kinetics and microstructure evolution during annealing of a cold-rolled Fe-Mn-C alloy. *Acta Materialia* 2011;59:3229-43. [DOI](#)

63. Lü Y, Hutchinson B, Molodov DA, Gottstein G. Effect of deformation and annealing on the formation and reversion of ε -martensite in an Fe-Mn-C alloy. *Acta Materialia* 2010;58:3079-90. [DOI](#)
64. Cho S, Yoo Y. Static recrystallization kinetics of 304 stainless steels. *J Mater Sci* 2001;36:4273-8. [DOI](#)
65. Ma B, Peng Y, Jia B, Liu Y. Static recrystallization kinetics model after hot deformation of low-alloy steel Q345B. *J Iron Steel Res Int* 2010;17:61-6. [DOI](#)
66. Lin Y, Chen M, Zhang J. Modeling of flow stress of 42CrMo steel under hot compression. *Mater Sci Eng A* 2009;499:88-92. [DOI](#)
67. Quan G, Mao A, Zou Z, Luo G, Liang J. Description of grain refinement by dynamic recrystallization under hot compressions for as-extruded 3Cr20Ni10W2 heat-resistant alloy. *High Temp Mater Proc* 2015;34:697-713. [DOI](#)
68. Curtze S, Kuokkala V. Dependence of tensile deformation behavior of TWIP steels on stacking fault energy, temperature and strain rate. *Acta Materialia* 2010;58:5129-41. [DOI](#)
69. Miyajima Y, Mitsuhashi M, Hata S, Nakashima H, Tsuji N. Quantification of internal dislocation density using scanning transmission electron microscopy in ultrafine grained pure aluminium fabricated by severe plastic deformation. *Mater Sci Eng A* 2010;528:776-9. [DOI](#)
70. Won JW, Lee T, Hong S, Lee Y, Lee JH, Lee CS. Role of deformation twins in static recrystallization kinetics of high-purity alpha titanium. *Met Mater Int* 2016;22:1041-8. [DOI](#)